Sr-Doping-Modulated Metal-Insulator Transition in $NdNiO_3$ Epitaxial Films

Huan Ye(叶欢)[1], Enda Hua(华恩达)[1], Fang Xu(许方)[1], Jingdi Lu(鲁京迪)[1], Feng Jin(金锋)[1], Wenbin Wu(吴文彬)[1], Liang, Si(司良)[2*], and Lingfei Wang(王凌飞)[1*]

[1]*Hefei National Research Center for Physical Sciences at Microscale, University of Science and Technology of China, Hefei 230026, China*
[2]*School of Physics, Northwest University, Xi'an 710127, China*

(Received 22 July 2024; accepted manuscript online 10 October 2024)

Perovskite-structured nickelates, $ReNiO_3$ (Re = rare earth), have long garnered significant research interest due to their sharp and highly tunable metal-insulator transitions (MITs). Doping the parent compound $ReNiO_3$ with alkaline earth metal can substantially suppress this MIT. Recently, intriguing superconductivity has been discovered in doped infinite-layer nickelates ($ReNiO_2$), while the mechanism behind A-site doping-suppressed MIT in the parent compound $ReNiO_3$ remains unclear. To address this problem, we grew a series of $Nd_{1-x}Sr_xNiO_3$ (NSNO, x = 0–0.2) thin films and conducted systematic electrical transport measurements. Our resistivity and Hall measurements suggest that Sr-induced excessive holes are not the primary reason for MIT suppression. Instead, first-principles calculations indicate that Sr cations, with larger ionic radius, suppress breathing mode distortions and promote charge transfer between oxygen and Ni cations. This process weakens Ni–O bond disproportionation and Ni^{2+}/Ni^{4+} charge disproportionation. Such significant modulations in lattice and electronic structures convert the ground state from a charge-disproportionated antiferromagnetic insulator to a paramagnetic metal, thereby suppressing the MIT. This scenario is further supported by the weakened MIT observed in the tensile-strained NSNO/$SrTiO_3$(001) films. Our work reveals the A-side doping-modulated electrical transport of perovskite nickelate films, providing deeper insights into novel electric phases in these strongly correlated nickelate systems.

DOI: 10.1088/0256-307X/41/11/117301

Perovskite-structured rare-earth nickelates ($ReNiO_3$) are featured by their pronounced and highly tunable metal-insulator transitions (MITs). As a typical electron correlation system, $ReNiO_3$ has a complex multiband electronic structure and strong coupling between lattice, charge, spin, and orbital degree of freedom.[1] Thanks to these features, $ReNiO_3$ has received considerable research interests in both fundamental and application aspects. On the one hand, the $ReNiO_3$-based oxide thin films and heterostructures display a vast array of intriguing correlated physics phenomena, including multiferroicity,[2–4] phase separation,[5–8] Mott physics,[9–12] charge-orbital ordering,[13–15] complex magnetic ordering,[16–20] and strain-induced self-doping,[21] etc. On the other hand, the MIT in $ReNiO_3$ can be effectively controlled by a variety of stimuli, thus enabling intriguing device applications, including electrochemical sensors, resistive switching memory devices, synaptic transistors, and perovskite fuel cells, etc.[22–27]

In $ReNiO_3$, the first-order phase transition from a paramagnetic-metal to antiferromagnetic-insulating is accompanied by a structural transition from orthorhombic to monoclinic. The driving force of this MIT relies on the electronic instability associated with the unstable 3+ valence state of the Ni cation, which leads to a charge disproportionation state: adjacent two Ni^{3+} cations split into one Ni^{2+} cation and one Ni^{4+} cation. The charge disproportionation further results in alternately expanded and compressed NiO_6 octahedra, the so-called breathing-mode distortion. The charge disproportionation is strongly correlated to the Ni–O bond length and Ni–O–Ni bond angle. Therefore, both the amplitude and temperature of MIT in $ReNiO_3$ can be engineered by the octahedral rotation pattern (OOP). In bulk, OOP is mainly determined by the ionic radius mismatch between A- and B-site cations.[13,28,29] In $ReNiO_3$-based epitaxial heterostructures, epitaxial strain,[11,30–33] dimension crossover,[34] and interfacial atomic structures[9,35–37] can be seen as effective tuning knobs for harnessing the MIT.

Very recently, intriguing superconductivity has been discovered in the doped infinite layer rare-earth nickelate thin film systems. In 2019, Li *et al.* observed robust superconductivity up to ∼9.1 K in Sr-doped infinite-layer $NdNiO_2$, which is prepared by chemically reducing the perovskite $NdNiO_3$ film with CaH_2.[38,39] The $Nd_{1-x}Sr_xNiO_2$ films exhibit a typical superconducting dome at $0.12 \leq x \leq 0.24$ and weak insulating states in both under-doped and over-doped regimes.[40] Although the superconductivity in the A-site doped infinite layer $ReNiO_2$ phase has been intensively investigated, only a few reports focus on the A-site doping effects in the parent perovskite $ReNiO_3$. Researchers found that both electron (Sr) and hole (Th)

*Corresponding authors. Email: siliang@nwu.edu.cn; wanglf@ustc.edu.cn
© 2024 Chinese Physical Society and IOP Publishing Ltd

doping can suppress the MIT in $NdNiO_3$ single crystal and thin films.[13,41–43] However, the detailed evolution of lattice and electronic structures with A-site doping levels has not been clarified. The origin of gradually suppressed MIT remains elusive. Further clarifying the doping effect is essential, not only for future device applications of perovskite nickelates but also for comprehensively understanding the superconductivity in infinite-layer nickelates.

In this Letter, we explore the Sr-doping modulated MIT in epitaxial $NdNiO_3$ thin films. We prepared a series of 12 nm $Nd_{1-x}Sr_xNiO_3$ (NSNO) films with various Sr doping levels x and systematically characterized their structure and electrical transport properties. As the Sr doping level increases from 0 to 0.2, the MIT can be gradually suppressed, accompanied by sizable changes in both hole carrier density and mobility. Incorporating the density functional theory (DFT) calculations, we further clarify that the MIT is strongly correlated to the breathing mode deformation of NiO_6 octahedra and charge disproportionation between neighboring Ni^{3+} cations. Both factors can be strongly influenced by the Sr doping. Our work provides essential guidelines for the A-site doping-modulated structure and electrical transport of perovskite nickelate films, which provide a deeper understanding of novel electric phases in these strongly correlated nickelate systems.

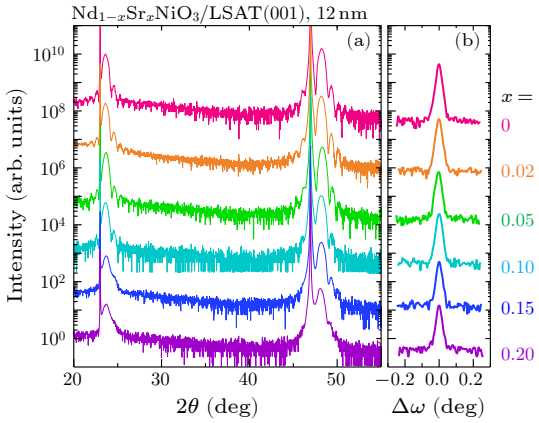

Fig. 1. Structural characterization of NSNO epitaxial thin films. (a) The XRD 2θ–ω linear scans near NSNO (004) diffractions, measured from 12 nm NSNO/LSAT(001) films with different Sr doping level x [LSAT: $(La_{0.3}Sr_{0.7})(Al_{0.65}Ta_{0.35})O_3$]. (b) The XRD ω-scans rocking curves of the NSNO(004) diffractions with sharp peaks.

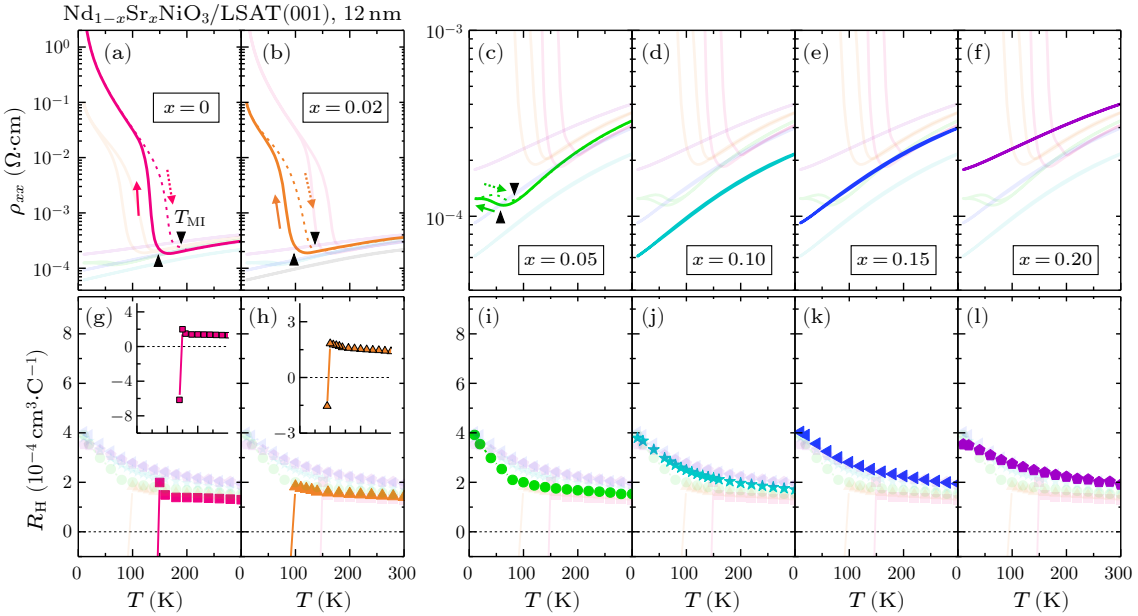

Fig. 2. Electrical transport properties of NSNO/LSAT(001) films. (a)–(f) Temperature-dependent resistivity (ρ_{xx}–T) of a series of NSNO/LSAT(001) films with Sr doping level x ranging from 0 to 0.20. The solid and dashed curves/arrows correspond to the cooling and heating processes, respectively. The metal-insulator transition temperature (T_{MI}) is also marked by solid triangles in (a)–(c). (g)–(l) T-dependent Hall coefficient (R_H) of the NSNO/LSAT(001) films with Sr doping level x ranging from 0 to 0.20. In (g) and (h), the insets are large-scale R_H–T curves, highlighting the sign change of R_H near T_{MI}.

We deposited a series of 12-nm-thick NSNO (x = 0–0.20) films on the (001)-oriented $(La_{0.3}Sr_{0.7})(Al_{0.65}Ta_{0.35})O_3$ [LSAT(001)] substrates using the pulsed laser deposition (PLD) method (see Method and Material for details of sample preparations). These NSNO films were deposited onto the LSAT(001) substrates by laser ablating the polycrystalline NSNO targets with a focused laser beam. During the NSNO film deposition, we maintained the laser fluence, substrate temperature, and oxygen partial pressure at 2 J/cm^2, 700°, and 20 Pa, respectively. These key parameters have been optimized according to earlier studies.[38,44] We first characterized the epitaxial quality of these NSNO/LSAT(001) films by x-ray diffraction (XRD). All of the 2θ–ω scans [Fig. 1(a)]

display well-defined NSNO(002) (at $\sim$23.6°) and (004) (at $\sim$48.2°) diffraction peaks only. This is consistent with the previous reports.[44] The sharp Laue fringes further suggest smooth surface and sharp heterointerfaces. Moreover, the full widths at half maximum (FWHMs) for all of the ω-scan rocking curves [Fig. 1(b)] measured near NSNO(004) diffractions are below 0.02°, further corroborating the high epitaxial quality of these films. We also characterized the epitaxial strain states of the NSNO/LSAT(001) films through reciprocal space mappings (RSMs) around the asymmetric LSAT (103) diffraction. As shown in Fig. S1 of the Supplementary Material, for all the films, the NSNO (206) diffraction shares the same in-plane reciprocal vectors (Q_x) as that of the LSAT (103) diffraction. Namely, all of the NSNO films are coherently and tensile strained to the LSAT(001) substrates.

Despite little impact on the epitaxial quality, Sr doping in NSNO/LSAT(001) films can strongly modulate the electrical transport properties. Figures 2(a)–2(e) show the temperature-dependent longitudinal resistivity (ρ_{xx}–T) curves of a series of 12-nm-thick NSNO/LSAT(001) films (x = 0–0.20). For the undoped NNO/LSAT(001) film [Fig. 2(a)], upon cooling, the ρ_{xx}–T curve first displays metallic behavior and then a steep increase in ρ_{xx} at $\sim$150 K ($T_{\rm MI}$), signifying a typical MIT. Upon warming, the MIT occurs at a higher $T_{\rm MI}$ of 190 K, giving rise to apparent thermal hysteresis behavior. For the NSNO/LSAT(001) film with $x = 0.02$, the hysteretic MIT persists in the ρ_{xx}–T curve, while the $T_{\rm MI}$ decreases to 100 K (cooling) and 130 K (warming) [Fig. 2(b)]. The ρ_{xx} in the insulating regime decreases by one order of magnitude compared to that in the NNO/LSAT(001) film, suggesting a sizable degradation in MIT. As x increases to 0.05, the ρ_{xx}–T curve displays a metallic behavior down to 60 K, following a weak MIT [Fig. 2(c)]. By further increasing x above 0.10, the ρ_{xx}–T curves [Figs. 2(d)–2(f)] exhibit metallic behavior over the entire T range. Namely, Sr doping can effectively suppress the MIT in NNO thin films.

To further probe the Sr doping-modulated electrical transport, we also conducted Hall measurements on these NSNO/LSAT(001) films. The magnetic field-dependent transverse resistivity (ρ_{xy}–H) curves are summarized in Fig. S2(b) in the Supplementary Material and the Hall coefficient ($R_{\rm H}$) derived from these ρ_{xy}–H curves are plotted as functions of temperature [Figs. 2(g)–2(l)]. Note that the ρ_{xx} of NNO and NSNO ($x = 0.02$) show pronounced relaxation behavior near $T_{\rm MI}$, and such time-dependent changes in ρ_{xx} can also crosstalk to the ρ_{xy}.[45,46] To precisely determine the $R_{\rm H}$, we employed an additional fitting procedure to deduct the relaxation-induced artifacts in $R_{\rm H}$ [Fig. S2(a)]. For all the NNO and NSNO films, in the metallic regime, the $R_{\rm H}$ values are positive and increase gradually upon cooling. Accordingly, the metallicity is dominated by hole conductivity. For the NNO and NSNO ($x = 0.02$) films, as the temperature decreases down to $T_{\rm MI}$, the $R_{\rm H}$ shows a sharp sign reversal from positive to negative, which is consistent with the previously reported transport results.[46–48] According to the angle-resolved photoemission spectroscopy (ARPES), in the metallic state of NNO, the small pocket at the Γ point is electron-like, while the larger pocket centered at the BZ diagonal (A point) is hole-like.[47] The positive sign of $R_{\rm H}$ in the paramagnetic-metal phase is due to the larger volume of the hole pocket than the electron pocket.[46,49,50] At low temperatures, the strong interaction between O 2p and Ni 3d in the compressed oxygen octahedron opens a gap on the Fermi surface of the hole due to charge disproportionation, contributing to the transport of the remaining electron pockets, resulting in the observed sign reversal of $R_{\rm H}$ below $T_{\rm MI}$.

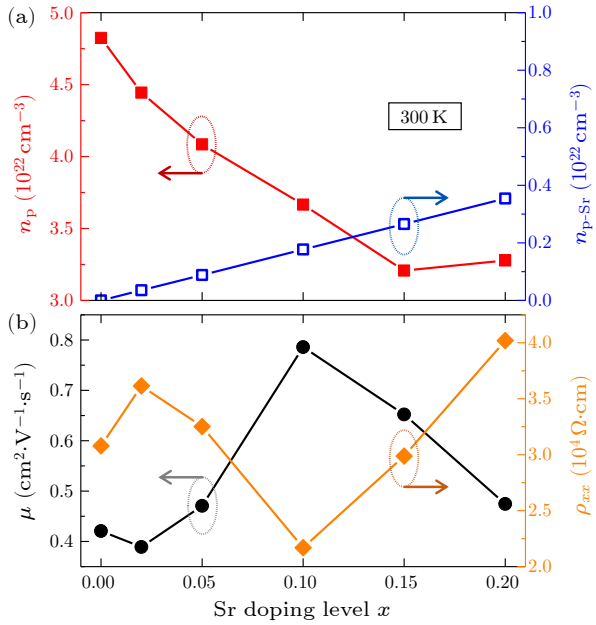

Fig. 3. Electrical transport parameters of the NSNO/LSAT(001) films. (a) Sr doping level (x) dependence of hole concentration ($n_{\rm p}$) at 300 K and Sr dopant-induced nominal hole concentration ($n_{\rm p\text{-}Sr}$). The hole concentration gradually decreases until it begins to increase at a doping level of 0.2. The nominal hole concentration ($n_{\rm p\text{-}Sr}$) obtained from Sr doping increases linearly with the Sr doping level x. However, its magnitude is about one order of magnitude smaller than the $n_{\rm p}$ value determined by Hall measurements. The decrease of carriers may be caused by immediate localized states induced by Sr dopants within the NNO band gap and the introduction of oxygen vacancies. (b) The x-dependent carrier mobility (μ) from Hall measurements and longitudinal resistivity (ρ_{xx}) at 300 K. The resistivity (ρ_{xx}) and mobility (μ) change nonmonotonically with x at 300 K. When $x = 0.02$, ρ_{xx} (μ) slightly increases (decreases), which may be related to the enhancement of hybridization between O 2p and Ni 3d bands due to the reduction of Ni–O–Ni bond angle by Sr doping. With the increase of Sr doping amount, ρ_{xx} (μ) of NSNO film first decreases (increases) and reaches a minimum (maximum) at $x = 0.1$.

To further understand the Sr-doping-controlled MIT in NSNO films, we plot the electrical transport parameters at 300 K as functions of Sr doping level x in Fig. 3(a). It is seen that the hole concentration ($n_{\rm p}$) decreases gradually as x increases from 0 to 0.15 and then increases slightly as x increases to 0.2. In sharp contrast, the nominal hole

concentration derived from the Sr doping ($n_{\text{p-Sr}}$, one hole for each Sr dopant) increases linearly with Sr doping level x, and the magnitude is approximately one order of magnitude smaller than the experimentally determined n_{p} value. This inconsistency strongly suggests that the Sr dopants do not directly introduce hole carriers into the conduction band, but rather induce immediate localized states within the NNO band gap.[51,52] Given a small $x = 0.02$, the intermediate localized state in the band gap results in a small increase in resistance [Fig. 3(b)]. As the Sr doping level x increases over 0.05, the in-gap states tend to spread and eventually merge with the valence band, resulting in a reduction of the band gap. Meanwhile, Sr doping may also introduce oxygen vacancies into the NSNO films,[53] thereby compensating some hole carriers and reducing the real hole concentration. Notably, since the $n_{\text{p-Sr}}$ is much smaller than n_{p}, the Sr-induced hole carriers should not be the direct cause of the suppressed MIT.

As shown in Fig. 3(b), the resistivity (ρ_{xx}) and mobility (μ) at 300 K change non-monotonically with x. Specifically, as x increases from 0 to 0.02, ρ_{xx} (μ) increases (decreases) slightly. This phenomenon may relate to the disorder caused by A-site Sr doping and the resulting valence variation of Ni cations. As the Sr doping level increases further, ρ_{xx} (μ) of the NSNO films first decreases (increases) and reaches the minimum (maximum) at $x = 0.1$. In the Sr doping range of $0.02 \leq x \leq 0.10$, the large ionic radius of Sr could result in two structural modulations. First, it effectively increases the Ni–O–Ni bond angle towards 180°, thus enhancing the hybridization between Ni $3d$ and O $2p$ orbitals. Second, it suppresses the breathing-mode phonon, reducing the phonon scattering of carriers. Both modulations can enhance μ and thus reduce ρ_{xx} till the MIT is fully suppressed at $x = 0.10$. With further increases x from 0.10 to 0.20, since the MIT is already suppressed, the disorder induced by heavy Sr doping dominates electrical transport, leading to a gradual increase in ρ_{xx} and a decrease in μ with higher x. As depicted in Figs. S3 and S4, the non-monotonic doping dependence of ρ_{xx} and μ persists at low temperatures.

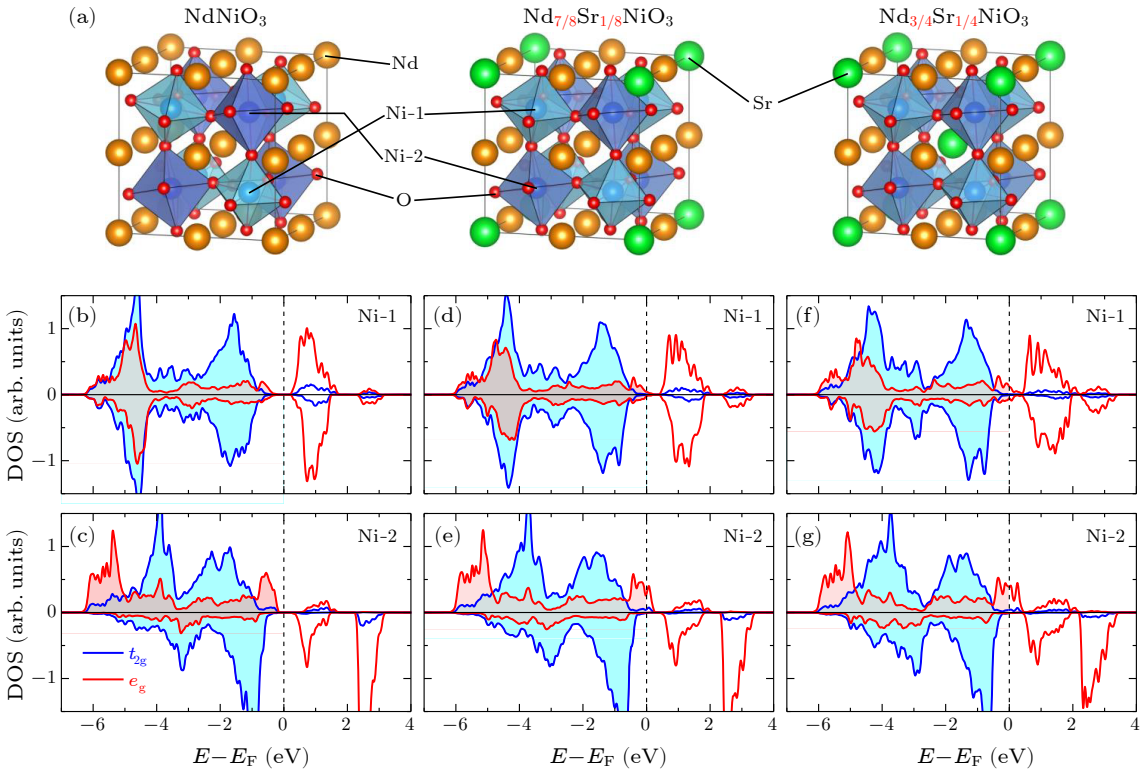

Fig. 4. First-principles calculations on the electron structures of NSNO. (a) Schematic diagram of $2 \times 2 \times 2$ NNO or NSNO ($x = 1/8$ and $1/4$) supercells for first-principles DFT calculations. The NiO_6 octahedral with different electronic states are colored by light or dark blue. The two types of Ni atoms are marked by Ni-1 and Ni-2, respectively. (b)–(g) DOS profiles of the Ni-1 and Ni-2 $3d$ orbitals computed for NNO and NSNO supercells. The Fermi level (E_{F}) is marked by dashed lines at 0 eV. The occupied DOS below E_{F} are labeled by filled regions. When $x = 0$ [(b), (c)], the spin-up and spin-down DOS of Ni-1 are almost identical, signifying a low spin state. For Ni-2, the spin-up and spin-down DOS are different, leading to a high spin state. For $x = 1/8$ [(d), (e)] and $1/4$ [(f), (g)], the charge transfer between Ni-1 and Ni-2 causes the e_{g} bands to shift upwards, resulting in the emergence of Ni-1 spin polarization.

According to our transport results, the suppressed MIT in NSNO films cannot be simply understood by the Sr-doping-introduced hole carriers. Therefore, we speculate that the suppression of MIT is correlated to the Sr doping-mediated modulations in both atomic structure and electronic structure. To clarify this scenario, we per-

form first-principles DFT calculations based on density-functional theory plus Coulomb interaction (DFT + U) framework. As shown in Fig. 4(a), we construct three $2 \times 2 \times 2$ NSNO supercells with nominal Sr concentration $x = 0$, 1/8, and 1/4 for calculation. To maintain the high symmetry of the atomic structure, we construct the NSNO supercell with $x = 1/8$ by replacing the eight Nd atoms at the apex corner. We further replace the central Nd atom with the Sr atom to construct the NSNO supercell with $x = 1/4$. The DFT-relaxed NNO and NSNO supercells show clear Ni–O bond disproportionation, which leads to the two types of NiO_6 octahedra. Here we label the compressed (shorter Ni–O bond) and expanded (longer Ni–O bond) octahedra as Ni-1 and Ni-2, respectively. The density-of-states (DOS) profiles of the NNO and NSNO supercells are included in Figs. 4(b)–4(g). The DFT-calculated supercell parameters, including the Ni–O–Ni bond angle, Ni–O bond length, valence, and local magnetic moments of Ni cations, are included in Fig. 5.

The DFT calculation reveals distinct electronic ground states of NNO and NSNO. Figures 4(b)–4(g) and Figs. S5 show the DOS profiles of Ni-1 and Ni-2 3d orbitals in the NNO and NSNO supercells. Positive and negative values of the DOS refer to spin-up and spin-down channels. The DOS near the Fermi surface is dominated by the Ni e_g band for all the NNO and NSNO supercells. For both the Ni-1 and Ni-2 cations in the NNO supercell, the DOSs for e_g orbitals are primarily unoccupied and well above the Fermi level (E_F), while the t_{2g} states (blue) are mostly filled below E_F, leading to a well-defined energy gap of 0.4 eV. For the Ni-1 case, the spin-up and spin-down DOSs are almost identical, signifying negligible spin-polarization. By contrast, the spin-up and spin-down DOSs for the Ni-2 cation are distinct, leading to considerable spin-polarization. For both the NSNO supercells with $x = 1/8$ and $x = 1/4$, the e_g bands shift upwards and result in unoccupied states, which is consistent with the Sr-induced hole doping. Namely, the ground states of NSNO are metallic, consistent with our experimental observations. The differences in spin-up and spin-down bands also reveal distinct spin-polarization between the Ni-1 and Ni-2 cations.

The DFT calculated atomic and electronic structures of NNO and NSNO supercells are summarized in Fig. 5. For the NNO supercell, the averaged Ni–O–Ni bond angle is 154.1° [Fig. 5(a)]. Such a considerable deviation from 180° can be attributed to the $a^-a^-c^+$ octahedral rotation pattern, stimulated by the ionic radius mismatch between Ni and Nd.[54] As shown in Figs. 5(b) and 5(c), the bond lengths (valence states) of Ni-1 and Ni-2 are 1.92 Å(+2.42) and 2.03 Å(+1.83). These results signify an obvious charge disproportionation of Ni^{3+} cations to Ni^{4+} $3d^6$ (Ni-1) and Ni^{2+} $3d^8$ (Ni-2) cations. For Ni-1, the short Ni–O bond gives rise to strong Ni–O hybridization, leading to the so-called $3d^8L^2$ state. In this case, the majority of holes are located at O p orbitals. The charge transfer from Ni-1 to Ni-2 cations also leads to a partially high-spin configuration in the Ni-2 cation [Fig. S6]. As shown in Fig. 5(d), the local moment of Ni-2 cation (m_{Ni}) in the NNO supercell is approximately 1.5 μ_B, while the m_{Ni} of Ni-1 is close to 0.

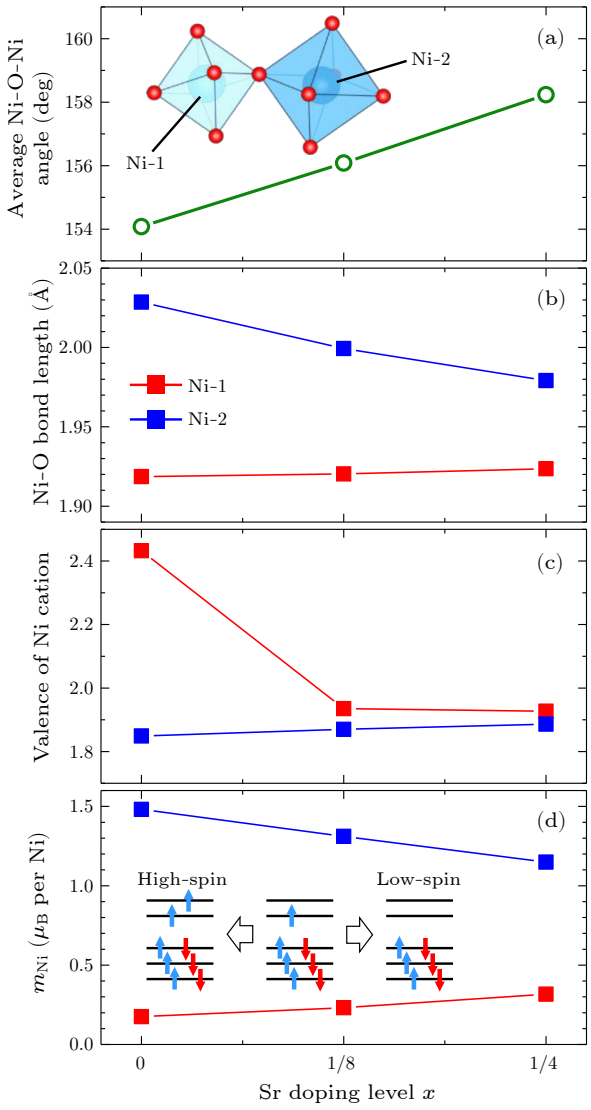

Fig. 5. Sr-doping controlled charge disproportionation of NNO and NSNO. (a)–(d) Sr doping level x dependent Ni–O–Ni angle (a), Ni–O bond length (b), Ni valence (c), and local moments at Ni sites (d). The inset in (a) is a schematic illustration of a pair of NiO_6 octahedra with charge disproportionation (Ni-1 and Ni-2). By introducing Sr doping, the Ni–O–Ni bond angle increases gradually probably due to the larger ionic radius of Sr. With increasing x, the Ni–O bond length of Ni-1 remains essentially unchanged, while the bond length of Ni-2 gradually decreases, indicating a weakening of the breathing mode distortion. The decrease of Ni-1 valence and the increase of Ni-2 valence suggest that Sr doping could facilitate the charge transfer from oxygen to Ni-1. The evolutions in bond lengths and bond angles reveal the mechanisms of bond/charge disproportionation. The inset in (d) is a schematic illustration of the high-spin (in Ni-2) and low-spin (in Ni-1) configurations triggered by charge disproportionation.

By introducing Sr doping, the Ni–O–Ni bond angle increases gradually, probably due to the larger ionic radius of Sr. As x increases, the Ni–O bond length of Ni-1 re-

mains nearly unchanged, while the bond length of Ni-2 decreases gradually, implying a weakened breathing mode distortion. The DFT computed valence of Ni-1 decreases dramatically from +2.43 ($x = 0$) to +1.95 ($x = 1/8$) and +1.91 ($x = 1/4$). On the contrary, the valence of Ni-2 only increases slightly to +1.85 ($x = 1/8$) and +1.88 ($x = 1/4$). Based on these results, we suggest that Sr doping could enable a charge transfer from oxygen to Ni-1, therefore weakening the charge and Ni–O bond disproportionation. This charge transfer also increases the m_{Ni} of Ni-1 and reduces the m_{Ni} of Ni-2. The metallic states of Ni-1 and Ni-2 at Sr-doping concentrations of $x = 1/8$ and $1/4$ are expected to reduce the super-exchange between the Ni-1–O–Ni-2 bond and enhance the strength of the double-exchange interaction. As a consequence, the AFM interaction between Ni cations is weakened while the FM interaction is enhanced, leading to the paramagnetic metal state after Sr-doping.

Based on the DFT calculation results, we can provide a clear picture of the Sr doping-suppressed MIT in NSNO films. For the undoped $NdNiO_3$, the system's ground state is a bond-disproportionated insulator, composed of longer and shorter Ni–O bonds. The electronic structures of Ni cations are composed of both $3d^8L^2$ and $3d^8$ configurations. Upon introducing Sr doping, several changes occur: Firstly, due to the larger ionic radius of Sr cations compared to Nd cations, some octahedra are compressed, shortening the Ni–O bond and suppressing the bond disproportionation mode. Secondly, the suppression of bond disproportionation reduces the difference in valence states between adjacent Ni cations. Thirdly, the Sr ions introduce hole doping, further assisting the formation of a metallic state. Concurrently, the Sr doping increases the Ni–O–Ni bond angle, which weakens the antiferromagnetic super-exchange interaction and enhances the double-exchange interaction. Such modulations in exchange interactions further assist the phase transition from a charge/bond disproportionated antiferromagnetic insulating state to a paramagnetic metallic state.

To further corroborate the above scenario, we grow a series of 12-nm-thick NSNO films on $SrTiO_3$(STO)(001) substrates. As depicted in Fig. S7 of the Supplementary Material, compared to the aforementioned LSAT(001) substrate, the STO(001) substrate can impose a larger in-plane tensile strain on the NSNO films. Such a tensile strain can homogeneously elongate the in-plane Ni–O bonds, thus suppressing the charge and Ni–O bond disproportionation modes. As shown in Figs. S8(a)–S8(d), given a fixed x, the MIT of NSNO/STO(001) films are considerably suppressed. At $x = 0.05$, the MIT disappears, and the μ reaches the maximum value [Fig. S8(e)]. These results are consistent with our aforementioned scenario. Namely, the tensile epitaxial strain plays a similar role as the Sr dopant, which can suppress the MIT by weakening the bond/charge disproportionation.

In summary, we have investigated the Sr-doping modulated MIT in NSNO epitaxial thin films. As the Sr doping level increases from 0 to 0.1, the MIT was gradually suppressed, accompanied by significant changes in both hole carrier density and mobility. Combining the electrical transport properties and DFT calculation results, we clarify that Sr-induced hole doping is not the main factor suppressing MIT. Instead, the Sr cations with larger ionic radius can suppress the breathing mode distortion and, consequently, the Ni–O bond disproportionation. Moreover, Sr doping triggers a charge transfer between oxygen and Ni cations, thereby suppressing the Ni^{2+}/Ni^{4+} charge disproportionation. These Sr-doping-induced structural and electronic modulations are responsible for the suppression of the MIT. This physical picture can be further supported by the weakened MIT in the tensile-strained NSNO/STO(001) films. Our work provides essential guidelines for understanding the doping-modulated electrical transport of perovskite nickelate films, facilitating the discovery and comprehension of novel electric phases in correlated nickelate systems.

Method and Material.

Synthesis of the Polycrystalline Ceramic Target and Epitaxial Films. The $Nd_{1-x}Sr_xNiO_3$ ($0 \le x \le 0.20$) polycrystalline bulk targets were using the solid-state reaction method. Powders of Nd_2O_3, NiO, and $SrCO_3$ were mixed in appropriate molar ratios. After grinding, the powder was heated at 1200° and 1300° for 12 h and then pressed into pellet form. Finally, the pellets were sintered at 1350° for 12 h. Here, 12 nm NSNO thin films were deposited on LSAT(001) single-crystal substrates by pulsed laser deposition technique using a KrF excimer laser ($\lambda = 248$ nm). The laser fluence used for ablating the target was about $2\,\mathrm{J\cdot cm^{-2}}$. The target-to-substrate distance was kept to be 50 mm, the substrate temperature was maintained at 700° and the oxygen atmosphere at 20 Pa during the sample growth. After deposition, the deposited films were annealed *in situ* under the growth condition for 10 min. Then we increased the oxygen pressure to 2 kPa at 400 ℃ and cooled the samples down to room temperature.

Structural and Electrical Characterizations. The high-quality epitaxial structures of the films were characterized by x-ray diffraction (XRD, PANalytical Empyrean x-ray diffractometer, Cu $K_{\alpha 1}$ radiation). The RSMs were collected on another diffractometer (Emperean, PanAlytical) with a 5-axis cradle. Resistance and Hall measurements were conducted using a physical properties measurement system (PPMS-14T, Quantum Design) at temperatures ranging from 10 to 300 K at a cooling/warming rate of 2 K/min. We used a linear four-point geometry with Pt top electrodes to make Ohmic contacts to measure the longitudinal resistance. To measure the Hall resistance, we patterned the film samples into Hall bars using photolithography. Hall coefficients were extracted from ±4 T field sweeps performed at a constant temperature. After removing the relaxation part and the longitudinal contribution, the linearly fitted slope is converted to the appropriate Hall coefficient units. A sample field scan performed at 140 K is shown in Fig. S2(b) of the Supplementary Material.

First-Principles Calculations. To simulate the Sr-doping effects on the structural, magnetic, and electronic properties of NNO, we performed first-principles calculations based on the density-functional theory

combined with on-site Coulomb interaction (DFT+U) framework.[55,56] A $2\times2\times2$ supercell of $NdNiO_3$ was initially constructed. Sr doping in NNO was achieved by replacing Nd atom(s) in the supercell with Sr, resulting in the chemical formula $Nd_{1-x}Sr_xNiO_3$ ($x = 0$, 1/8, and 1/4). Achieving higher experimental concentrations would require a much larger supercell, which poses challenges for DFT computational capacity.

Structural relaxations and density of states (DOS) calculations were performed using the VASP code[57] within the PBE version of the generalized gradient approximation (GGA)[58] on a dense $7\times7\times7$ k-mesh. For benchmarking, the Wien2k code[59,60] within PBE was employed. The interaction parameters for Ni-3d orbitals, obtained from constrained random phase approximation (cRPA) calculations,[61] have been validated: intra-orbital $U = 4.4\,\text{eV}$, Hund's exchange $J = 0.65\,\text{eV}$, and inter-orbital $V = U - 2J = 3.3\,\text{eV}$.[62]

Before computing the DOS, structural relaxations were performed for both non-magnetic and A-type antiferromagnetic orders of NNO and NSNO supercells. The differences in lattice constants between experimental and theoretical values were within 0.5%. Similar calculations with the in-plane lattice constants set to those of the LSAT(001) substrate did not result in significant changes. The relaxed crystal structures are shown in Fig. 4(a), visualized using the VESTA code.[63] Detailed structural parameters of the relaxed structures, including the Ni–O–Ni angle, Ni–O bond length, Ni valence, and local moments at Ni sites, were calculated for both non-magnetic and A-type antiferromagnetic orders and are presented in Figs. 4, 5, and Fig. S4 of the Supplementary Material.

Acknowledgements. This work was supported by the National Key Research and Development Program of China (Grant Nos. 2023YFA1406404 and 2020YFA0309100), the National Natural Science Foundation of China (Grant Nos. 12074365, 12374094, 12304153, U2032218, and 11974326), CAS Project for Young Scientists in Basic Research (Grant No. YSBR-084), the Fundamental Research Funds for the Central Universities (Grant Nos. WK9990000102 and WK2030000035), Anhui Provincial Natural Science Foundation (Grant No. 2308085MA15), Hefei Science Center CAS Foundation (Grant Nos. 2021HSC-CIP017 and 2016HSC-IU06), the National Natural Science Foundation of China (Grant No. 12274120), the China Postdoctoral Science Foundation (Grant No. 2022M713060). The sample fabrication was partially carried out at the USTC Center for Micro and Nanoscale Research and Fabrication. L. S. acknowledges the starting funds from Northwest University, and support from the Vienna Scientific Cluster (VSC) for the first-principles calculations.

References

[1] Mizokawa T and Fujimori A 2000 *Spin, Charge, And Orbital Ordering in 3d Transition-Metal Oxides Studied by Model Hartree–Fock* (Boston, MA: Springer) p 121
[2] Giovannetti G, Kumar S, Khomskii D, Picozzi S, and van den Brink J 2009 *Phys. Rev. Lett.* **103** 156401
[3] Ardizzone I, Teyssier J, Crassee I, Kuzmenko A B, Mazzone D G, Gawryluk D J, Medarde M, and van der Marel D 2021 *Phys. Rev. Res.* **3** 033007
[4] Binci L, Kotiuga M, Timrov I, and Marzari N 2023 *Phys. Rev. Res.* **5** 033146
[5] Patel R K, Meyers D, Liu X R, Mandal P, Kareev M, Shafer P, Kim J W, Ryan P J, Middey S, and Chakhalian J 2020 *APL Mater.* **8** 041113
[6] Mattoni G, Zubko P, Maccherozzi F, van der Torren A J H, Boltje D B, Hadjimichael M, Manca N, Catalano S, Gibert M, Liu Y, Aarts J, Triscone J M, Dhesi S S, and Caviglia A D 2016 *Nat. Commun.* **7** 13141
[7] Kumar D, Rajeev K P, Kushwaha A K, and Budhani R C 2010 *J. Appl. Phys.* **108** 063503
[8] Kim T H, Angst M, Hu B, Jin R, Zhang X G, Wendelken J F, Plummer E W, and Li A P 2010 *Proc. Natl. Acad. Sci. USA* **107** 5272
[9] Middey S, Chakhalian J, Mahadevan P, Freeland J W, Millis A J, and Sarma D D 2016 *Annu. Rev. Mater. Res.* **46** 305
[10] Park H, Millis A J, and Marianetti C A 2012 *Phys. Rev. Lett.* **109** 156402
[11] Liu J, Kargarian M, Kareev M, Gray B, Ryan P J, Cruz A, Tahir N, Chuang Y D, Guo J, Rondinelli J M, Freeland J W, Fiete G A, and Chakhalian J 2013 *Nat. Commun.* **4** 2714
[12] Liu J, Okamoto S, van Veenendaal M, Kareev M, Gray B, Ryan P, Freeland J W, and Chakhalian J 2012 *Phys. Rev. B* **86** 079904
[13] Alonso J A, García-Muñoz J L, Fernández-Díaz M T, Aranda M A G, Martínez-Lope M J, and Casais M T 1999 *Phys. Rev. Lett.* **82** 3871
[14] Vambold N O, Sazhaev G A, and Leonov I V 2023 *JETP Lett.* **118** 886
[15] Yamauchi K and Hamada I 2023 *Phys. Rev. B* **108** 045108
[16] Caviglia A D, Först M, Scherwitzl R, Khanna V, Bromberger H, Mankowsky R, Singla R, Chuang Y D, Lee W S, Krupin O, Schlotter W F, Turner J J, Dakovski G L, Minitti M P, Robinson J, Scagnoli V, Wilkins S B, Cavill S A, Gibert M, Gariglio S, Zubko P, Triscone J M, Hill J P, Dhesi S S, and Cavalleri A 2013 *Phys. Rev. B* **88** 220401
[17] Domínguez C, Georgescu A B, Mundet B, Zhang Y, Fowlie J, Mercy A, Waelchli A, Catalano S, Alexander D T L, Ghosez P, Georges A, Millis A J, Gibert M, and Triscone J M 2020 *Nat. Mater.* **19** 1182
[18] Domínguez C, Fowlie J, Georgescu A B, Mundet B, Jaouen N, Viret M, Suter A, Millis A J, Salman Z, Proksch T, Gibert M, and Triscone J M 2023 *Phys. Rev. Mater.* **7** 065002
[19] Chen D, Worm P, Si L, Zhang C, Deng F, Jiang P, and Zhong Z 2023 *Chin. Phys. B* **32** 087105
[20] Zhang M, Zhang Y, Guo H, and Yang F 2021 *Chin. Phys. B* **30** 108204
[21] Moon E J, Rondinelli J M, Prasai N, Gray B A, Kareev M, Chakhalian J, and Cohn J L 2012 *Phys. Rev. B* **85** 121106
[22] Zhang Z, Schwanz D, Narayanan B, Kotiuga M, Dura J A, Cherukara M, Zhou H, Freeland J W, Li J, Sutarto R, He F, Wu C, Zhu J, Sun Y, Ramadoss K, Nonnenmann S S, Yu N, Comin R, Rabe K M, Sankaranarayanan S K R S, and Ramanathan S 2018 *Nature* **553** 68
[23] Sivakumar M, Pandi K, Chen S M, Cheng Y H, and Sakthivel M 2017 *New. J. Chem.* **41** 11201
[24] Park T J, Selcuk K, Zhang H T, Manna S, Batra R, Wang Q, Yu H, Aadit N A, Sankaranarayanan S K R S, Zhou H, Camsari K Y, and Ramanathan S 2022 *Nano Lett.* **22** 8654
[25] Shi J, Ha S D, Zhou Y, Schoofs F, and Ramanathan S 2013 *Nat. Commun.* **4** 2676
[26] Oh C, Heo S, Jang H M, and Son J 2016 *Appl. Phys. Lett.* **108** 122106

[27] Zhou Y, Guan X, Zhou H, Ramadoss K, Adam S, Liu H, Lee S, Shi J, Tsuchiya M, Fong D D, and Ramanathan S 2016 *Nature* **534** 231
[28] Torrance J, Lacorre P, Nazzal A, Ansaldo E, and Niedermayer C 1992 *Phys. Rev. B* **45** 8209
[29] Medarde M L 1997 *J. Phys.: Condens. Matter* **9** 1679
[30] Catalano S, Gibert M, Bisogni V, Peil O E, He F, Sutarto R, Viret M, Zubko P, Scherwitzl R, Georges A, Sawatzky G A, Schmitt T, and Triscone J M 2014 *APL Mater.* **2** 116110
[31] Liu J, Kareev M, Gray B, Kim J W, Ryan P, Dabrowski B, Freeland J W, and Chakhalian J 2010 *Appl. Phys. Lett.* **96** 233110
[32] Frano A, Schierle E, Haverkort M W, Lu Y, Wu M, Blanco-Canosa S, Nwankwo U, Boris A V, Wochner P, Cristiani G, Habermeier H U, Logvenov G, Hinkov V, Benckiser E, Weschke E, and Keimer B 2013 *Phys. Rev. Lett.* **111** 106804
[33] Hepting M, Minola M, Frano A, Cristiani G, Logvenov G, Schierle E, Wu M, Bluschke M, Weschke E, Habermeier H U, Benckiser E, Le Tacon M, and Keimer B 2014 *Phys. Rev. Lett.* **113** 227206
[34] Boris A V, Matiks Y, Benckiser E, Frano A, Popovich P, Hinkov V, Wochner P, Castro-Colin M, Detemple E, Malik V K, Bernhard C, Prokscha T, Suter A, Salman Z, Morenzoni E, Cristiani G, Habermeier H U, and Keimer B 2011 *Science* **332** 937
[35] Benckiser E, Haverkort M W, Brück S, Goering E, Macke S, Frañó A, Yang X, Andersen O K, Cristiani G, Habermeier H U, Boris A V, Zegkinoglou I, Wochner P, Kim H J, Hinkov V, and Keimer B 2011 *Nat. Mater.* **10** 189
[36] Disa A S, Kumah D P, Malashevich A, Chen H, Arena D A, Specht E D, Ismail-Beigi S, Walker F J, and Ahn C H 2015 *Phys. Rev. Lett.* **114** 026801
[37] Chen H, Kumah D P, Disa A S, Walker F J, Ahn C H, and Ismail-Beigi S 2013 *Phys. Rev. Lett.* **110** 186402
[38] Li D, Lee K, Wang B Y, Osada M, Crossley S, Lee H R, Cui Y, Hikita Y, and Hwang H Y 2019 *Nature* **572** 624
[39] Huang B 2023 *Chin. Phys. Lett.* **40** 057403
[40] Li D, Wang B Y, Lee K, Harvey S P, Osada M, Goodge B H, Kourkoutis L F, and Hwang H Y 2020 *Phys. Rev. Lett.* **125** 027001
[41] Alonso J A, MartíNez-Lope M J, and Hidalgo M A 1995 *J. Solid State Chem.* **116** 146
[42] Wang B X, Zheng H, Krivyakina E, Chmaissem O, Lopes P P, Lynn J W, Gallington L C, Ren Y, Rosenkranz S, Mitchell J F, and Phelan D 2020 *Phys. Rev. Mater.* **4** 084409
[43] Wang L, Chang L, Yin X, Rusydi A, You L, Zhou Y, Fang L, and Wang J 2017 *J. Phys.: Condens. Matter* **29** 025002
[44] Lee K, Goodge B H, Li D, Osada M, Wang B Y, Cui Y, Kourkoutis L F, and Hwang H Y 2020 *APL Mater.* **8** 041107
[45] Ojha S K, Ray S, Das T, Middey S, Sarkar S, Mahadevan P, Wang Z, Zhu Y, Liu X, Kareev M, and Chakhalian J 2019 *Phys. Rev. B* **99** 235153
[46] Hauser A J, Mikheev E, Moreno N E, Cain T A, Hwang J, Zhang J Y, and Stemmer S 2013 *Appl. Phys. Lett.* **103** 182105
[47] Song Q, Doyle S, Pan G A, El Baggari I, Ferenc Segedin D, Córdova Carrizales D, Nordlander J, Tzschaschel C, Ehrets J R, Hasan Z, El-Sherif H, Krishna J, Hanson C, Labollita H, Bostwick A, Jozwiak C, Rotenberg E, Xu S Y, Lanzara A, N'Diaye A T, Heikes C A, Liu Y H, Paik H, Brooks C M, Pamuk B, Heron J T, Shafer P, Ratcliff W D, Botana A S, Moreschini L, and Mundy J A 2023 *Nat. Phys.* **19** 522
[48] Hauser A J, Mikheev E, Moreno N E, Hwang J, Zhang J Y, and Stemmer S 2015 *Appl. Phys. Lett.* **106** 092104
[49] Dhaka R S, Das T, Plumb N C, Ristic Z, Kong W, Matt C E, Xu N, Dolui K, Razzoli E, Medarde M, Patthey L, Shi M, Radović M, and Mesot J 2015 *Phys. Rev. B* **92** 035127
[50] Eguchi R, Chainani A, Taguchi M, Matsunami M, Ishida Y, Horiba K, Senba Y, Ohashi H, and Shin S 2009 *Phys. Rev. B* **79** 115122
[51] Jiang J, Lee A T, Lee S, Lau C, Li M, Pedersen T M, Liu C, Gorovikov S, Zhdanovich S, Damascelli A, Zou K, Walker F J, Ismail-Beigi S, and Ahn C H 2021 *Phys. Rev. B* **103** 195153
[52] Liu Q, Dalpian G M, and Zunger A 2019 *Phys. Rev. Lett.* **122** 106403
[53] Iwasaki K, Ito T, Nagasaki T, Arita Y, Yoshino M, and Matsui T 2008 *J. Solid State Chem.* **181** 3145
[54] Rondinelli J M and Fennie C J 2012 *Adv. Mater.* **24** 1961
[55] Hohenberg P and Kohn W 1964 *Phys. Rev.* **136** B864
[56] Anisimov V I, Zaanen J, and Andersen O K 1991 *Phys. Rev. B* **44** 943
[57] Kresse G and Furthmüller J 1996 *Phys. Rev. B* **54** 11169
[58] Perdew J P, Burke K, and Ernzerhof M 1996 *Phys. Rev. Lett.* **77** 3865
[59] Blaha P, Schwarz K, Madsen G K H, Kvasnicka D, Luitz J and Schwarz K 2001 *Wien2k, An Augmented Plane Wave+ Local Orbitals Program for Calculating Crystal Properties* (Austria: Vienna University of Technology)
[60] Schwarz K, Blaha P, and Madsen G K H 2002 *Comput. Phys. Commun.* **147** 71
[61] Miyake T and Aryasetiawan F 2008 *Phys. Rev. B* **77** 085122
[62] Si L, Xiao W, Kaufmann J, Tomczak J M, Lu Y, Zhong Z, and Held K 2020 *Phys. Rev. Lett.* **124** 166402
[63] Momma K and Izumi F 2008 *J. Appl. Crystallogr.* **41** 653